
SPATIALLY-RESOLVED COHERENCE OF ORGANIC MOLECULAR SPINS AT ROOM-TEMPERATURE

Adrian Mena¹

Nicholas P. Sloane¹

Max R. Bonengel¹

Dane R. McCamey*¹

¹ School of Physics, UNSW Sydney, Sydney, 2052, NSW, Australia

ABSTRACT

Molecular spins are a versatile platform for quantum sensing. Not only are the spin-bearing molecules themselves widely tunable, they are also capable of being used as sensors as crystals, films and in solution. Using thin-films offers the advantages of high doping ratios and the ability to control the thickness with nanometre precision, however they also introduce disorder to the system. High proximity sensing can also be realised by using micro- and nano-crystals, however in many solid-state systems this leads to a reduction in coherence. In this paper we combine room-temperature optically-detected coherent control of molecular spins and microscopy to image the coherence properties of both thin-films and micro-crystals of pentacene doped *p*-terphenyl. In thin-films we find large amounts of variation in both the contrast and coherence times, leading to a variability in the magnetic field sensitivity of approximately 7.6 %. Applying the technique to micro-crystals shows much lower sensitivity variability (1.3 %), and we find no evidence of coherence loss toward the edge of the crystal. Finally we perform optically-detected coherent control on a nano-crystal, showing minimal loss in coherence and contrast compared to the bulk crystal, with a coherence time of 1.09 μ s and a contrast of 25 %.

1 Introduction

Optically addressable electronic spins have enabled high precision metrology, with measurements of magnetic fields[42], electric fields[12, 5], crystallographic strain[11] and temperature[34] below what can be achieved classically. Defects in crystalline solids such as nitrogen vacancies (NV)[10] in diamond and silicon carbide vacancies[9, 30] have enabled the development of room temperature, as their quantum states support long coherence times and high optical contrasts. This has allowed for the study of a range of phenomena, from biological processes[45, 47], to imaging current densities across semiconducting devices[39, 32, 44], furthering our understanding of microscopic processes. Alongside improving sensitivity, quantum sensors have focused on improving spatial resolution for imaging by reducing the distance from sensor to target, for example via the use of shallow-doped diamonds[24]. Further developments have enabled the miniaturisation of detectors, pushing our imaging capabilities to smaller scale, for example by utilising NV centres embedded in nanodiamonds to study thermal processes within single cells[22, 14]. Although the three dimensional crystal structure of these materials lead to well protected quantum states, their crystallinity creates a physical barrier preventing these devices from reaching the nanometer scale and their integration into nanoscale structures. Motivated by the desire for higher proximity measurements with smaller probes, alternative materials have gained considerable interest, such as defects in the two-dimensional van der Waals (vdW) material hexagonal boron nitride (hBN)[17, 37], and one-dimensional vdW materials such as boron-nitride nanotubes[15]. Following from the same motivation, a growing interest in molecular spins for quantum sensing has developed due to their inherent flexible deployment, providing a potential avenue to quantum sensing with thin-films, crystals, solutions and functionalised spin-bearing probes.

Spin bearing molecules make up a versatile sensing platform, with a number of spin systems including photo-excited metastable triplets[29, 26], molecular colour centres with ground state triplets[20, 21, 8, 6], coupled multi-spin systems[16] and engineered fluorescent proteins[13, 1]. Recently molecular spins have been explored as room-temperature quantum sensors for magnetometry[33, 23] and thermometry[34, 18]. A key benefit of molecules is that they are inherently nanoscale, enabling their integration into structures such as proteins with a reduced impact on their structure and dynamics[7]. These spin systems can be deployed in 3D crystalline structures or as evaporated thin-films, with the later as a potential method for achieving high resolution sensing. Doped crystals offer well protected quantum states, however thin-films are particularly attractive for imaging as they can be grown with nanometer precision[19] and with a high density of spin-bearing dopant molecules[25]. The trade-off for this over their crystalline counter-parts comes from the introduction of disorder, which has the potential to impact the uniformity of the film's sensitivity and therefore the imaging capability. In this paper we combine room-temperature optically detected coherent control of molecular spins with wide-field microscopy to characterise the sensitivity of both disordered thin-films and crystalline sensors. This investigation aims to understand the different approaches to deploying molecular spins as quantum sensors and guide efforts towards their use in high-proximity quantum sensing.

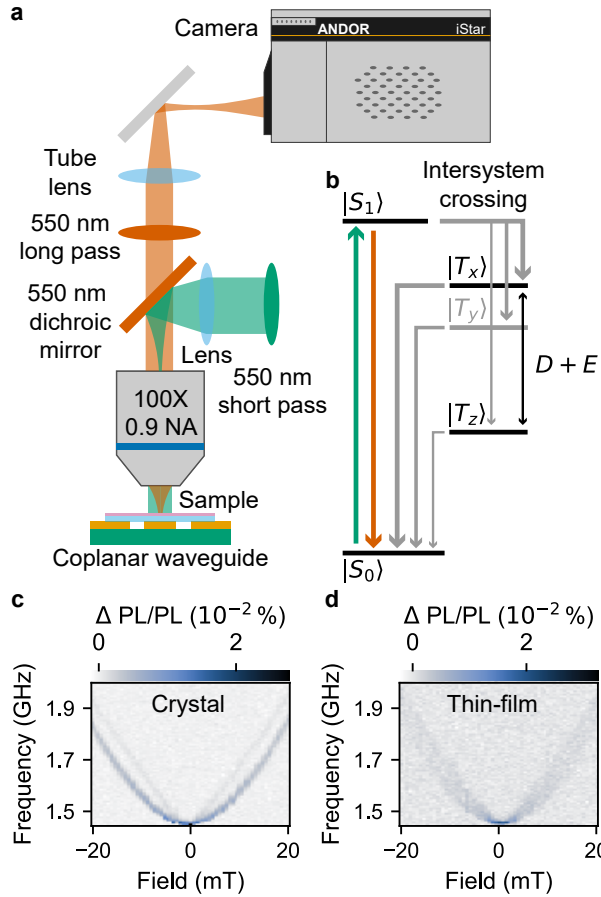


Figure 1: **Optically detected magnetic resonance with organic triplets.** a) Schematic of the setup used for spatially resolved optically detected magnetic resonance, including a microwave source, optical excitation, emission, optics for imaging and a camera used to perform spatially resolved measurements. b) Energy structure for pentacene, with a singlet ground and excited state. The lowest lying triplet is an excited state which can be populated via intersystem crossing. The triplet states are spin-1 and have microwave addressable transitions. A field-frequency sweep of the $|T_x\rangle \leftrightarrow |T_z\rangle$ transition can be seen in c) and d) for the crystal and film respectively.

We explore this with a staple system when it comes to molecular spins, pentacene doped in *p*-terphenyl. Figure 1a shows the essential elements of our experiments; Our sample is mounted on a co-planar waveguide (CPW) which is used to generate microwave frequency fields. The excitation, by a 520 nm laser, is focused on the back focal plane of the microscope objective, allowing for a flat illumination across the field of view. We collect the photoluminescence, imaging it onto a sCMOS camera which allows us to perform a spatially-resolved optically detected coherent control

measurement. This technique allows for parallel readout of a region of either thin-film or crystal samples, providing a rapid testbed to study the coherence properties across both ordered and disordered sensing substrate. Further details regarding the experimental setup can be found in the methods section.

Figure 1b contains a diagram of the key elements that enable optically detected magnetic resonance (ODMR) in pentacene doped *p*-terphenyl (pc:ptp). Photoexcitation drives the singlet ground state ($|S_0\rangle$) into the singlet excited state ($|S_1\rangle$). Either fluorescence back to $|S_0\rangle$ or intersystem crossing into the triplet manifold can occur from $|S_1\rangle$. The triplets generated from intersystem crossing are spin polarised due to anisotropic intersystem crossing rates, with probabilities $P_x : P_y : P_z = 0.76 : 0.16 : 0.08$ for the $|T_x\rangle$, $|T_y\rangle$ and $|T_z\rangle$ triplet sublevels respectively[35]. Likewise the depopulation rates are also anisotropic, with the decay rates (k_i) such that $k_x > k_y > k_z$, translating spin-populations into a triplet lifetime. Magnetic resonance, driven by a microwave field tuned to the energy splitting between two triplet sublevels, alters these spin state populations. This results in a change in the effective triplet lifetime, as for example shorter lived populations get shuffled into longer lived counterparts, this in turn alters the optical yield, enabling optical detected magnetic resonance (ODMR).

We use the setup to study both crystalline and disordered samples, using thermally evaporated thin-films and crystalline samples respectively. Figure 1c, d show the ODMR response of a crystal and film respectively when sweeping both field and microwave frequency about the $|T_x\rangle \leftrightarrow |T_z\rangle$ transition. We see in the crystalline sample the zero field transition splits into two peaks, whilst in the disordered thin-film the peak broadens into a powder spectra. The difference in these two samples highlights their structure, with the crystalline sample showing a high degree of order leading to only two distinct orientations of the pentacene molecules in the *p*-terphenyl host and the film having a partially oriented structure with many different pentacene orientations[25]. Simulations of the ODMR considering the molecular ordering for both samples can be found in the supplemental information.

2 Results

3 Spatially resolved coherent control of a molecular thin-film

Thin-films are an attractive approach to achieve high proximity quantum imaging, given that films can be reliably fabricated with nanometre precision [19]. This reduces the distance from the sensor to the target, allowing for the detection of smaller fields and an improvement in spatial resolution[1]. Additionally films are not limited to planar targets and evaporation can be performed onto non-planar substrates, allowing for 3 dimensional structures to be imaged. The trade-off here comes from the introduced disorder into the system, which will cause variation in the spin properties within the sensing layer and a non-uniform sensitivity[28, 31]. To understand the impact of disorder we apply a spatially resolved Hahn echo to a thermally evaporated thin-film of pentacene doped *p*-terphenyl (100 nm thickness, doped at 1%).

Figure 2a shows a histogram of the measurement contrasts across the film, with an average contrast of 0.55 % and a standard deviation of 0.05 %, leading to a variation of 9.8 %. The variation across the device is imaged in figure 2d, with the image showing the deviation in contrast ($C_{\text{dev}}^{(i,j)} = C^{(i,j)} / C_{\text{avg}}$) as a function of position. We note that the reported contrasts are significantly lower than previous reports for pentacene:*p*-terphenyl[29, 33]. This is a consequence of our wide-field measurement technique rather than the film, we see a similar reduction in absolute contrast in the crystal samples below and in figure 4 we see that when measured confocally the contrast is drastically improved.

Figure 2b shows the histogram for the coherence time, T_2 , across our film. Here we find an average of 890 ns with a standard deviation of 70 ns giving a variation of 7.9 %. The corresponding deviation map is shown in 2e, again clustering is observed here in the deviation across the device. Our average results agree with previously reported films, however the variation highlights the impact of disorder on the spin properties across our device, resulting in large variations of both contrast and coherence times.

Given that for our excited state triplet the sensitivity is inversely proportional to both measurement contrast and coherence time[4], we can assess the impact of variation in contrast and coherence on the sensitivity of our film. We define a sensitivity adjustment factor, η_{rel} , such that the sensitivity at a given point in the film is $\eta^{(i,j)} = \eta_{\text{rel}}^{(i,j)} \cdot \eta_{\text{avg}}$, where η_{avg} is the average sensitivity of the film and $\eta_{\text{rel}}^{(i,j)}$ is the local scale factor leading to an adjusted sensitivity, $\eta^{(i,j)}$, for a given point (i, j) in the film (full calculation procedure can be found in the methods section). Figure 2c shows the histogram of scale factors (η_{rel}) across our film, with variability of 7.6 %.

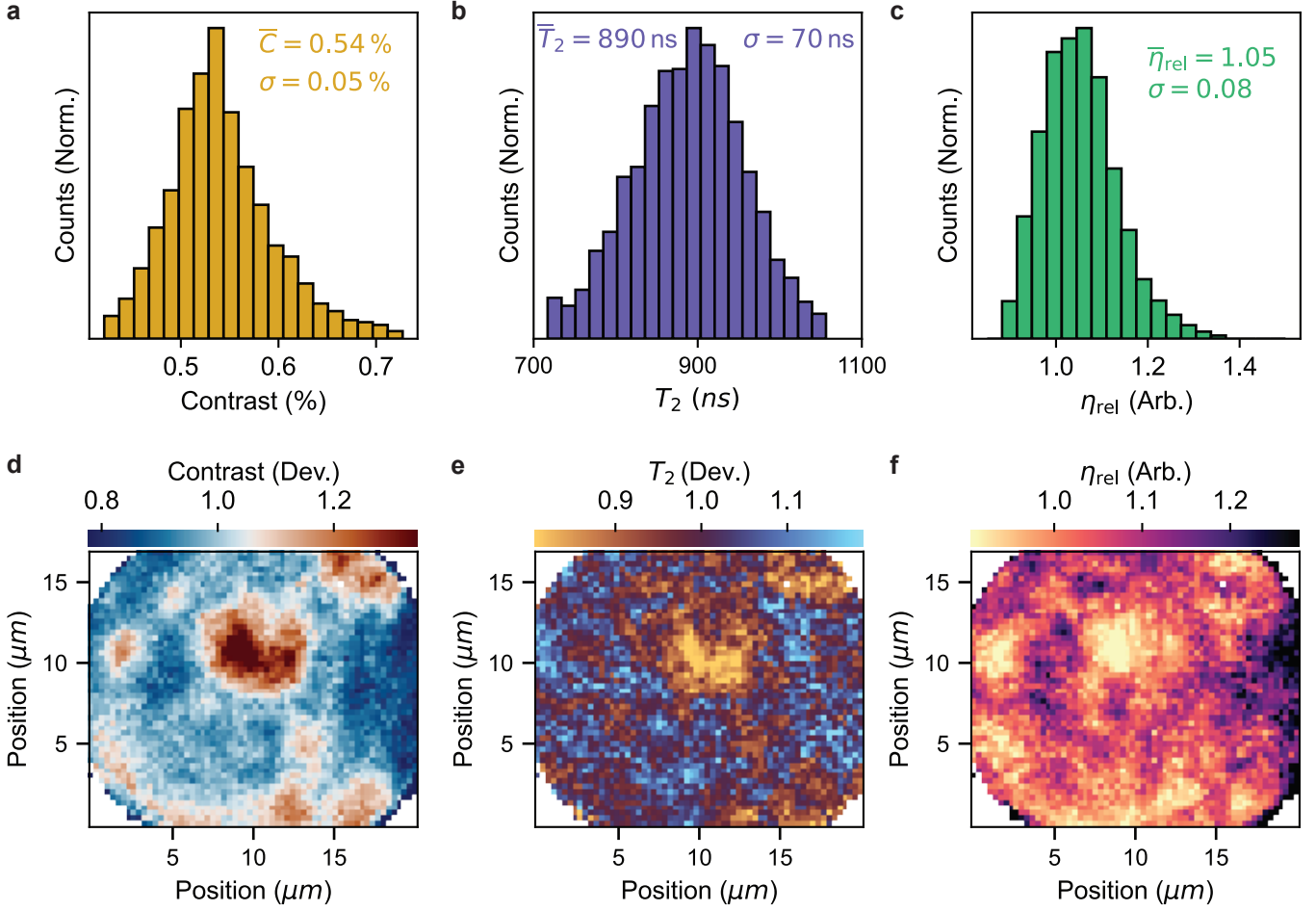


Figure 2: Spatially resolved coherent control of a thin-film. a) Histogram of the Hahn-echo measurement contrast across the film. b) Histogram of the coherence times, T_2 , measured across the film using an optically detected Hahn-echo. c) Histogram of the sensitivity scale factors found by calculating the impact of contrast and coherence time variation in the film. d) Spatial map of the deviation in measurement contrast. e) Spatial map of the deviation in coherence time. f) Spatial map of the deviation in sensitivity scale factor.

4 Spatially resolved coherent control of a molecular micro-crystal

Next we apply spatially resolved coherent control to an ordered system, using liquid phase exfoliation[2, 3], we produce micro-flakes of pentacene:*p*-terphenyl. These flakes are formed by sonicating a crystal with 0.1 % pentacene concentration in acetone. The flakes are drop-cast onto a quartz slide and we isolate an individual flake to resolve its' spin properties. Figure 3a shows the photoluminescence of the flake used in the experiment.

Using the Hahn-echo sequence we are able to image both the coherence time and measurement contrast across the crystal. Figure 3f shows the resulting T_2 map and the corresponding histogram is in figure 3b. We find an average T_2 of $1.17 \mu\text{s}$ with a variation of 1 %. The map shows an unexpected trend, with the edge of the crystal having a longer coherence time than the centre. To confirm this we average the measured coherence time with varying radial distances from the centre of the crystal (the radial distance (R) is indicated in figure 3b). Figure 3e shows the averaged T_2 plotted against the radial distance, with a clear trend that the edge of the crystal has a longer coherence time.

The measurement contrasts and the corresponding deviation map can be found in figures 3c and g respectively. Here we find an average contrast of 0.96 % with variation of 0.5 %. Both the contrast and coherence time show less variation than in the film, suggesting that the disorder of the film is a key contributor to the variations in sensitivity and coherence. Our work also highlights the importance of considering the environment of the spin-bearing molecules when designing molecular quantum technologies[41]. Here we show that by changing the ordering of the same dopant-host system we start to see significantly varied spin properties across our devices. Therefore, finding suitable host molecules that

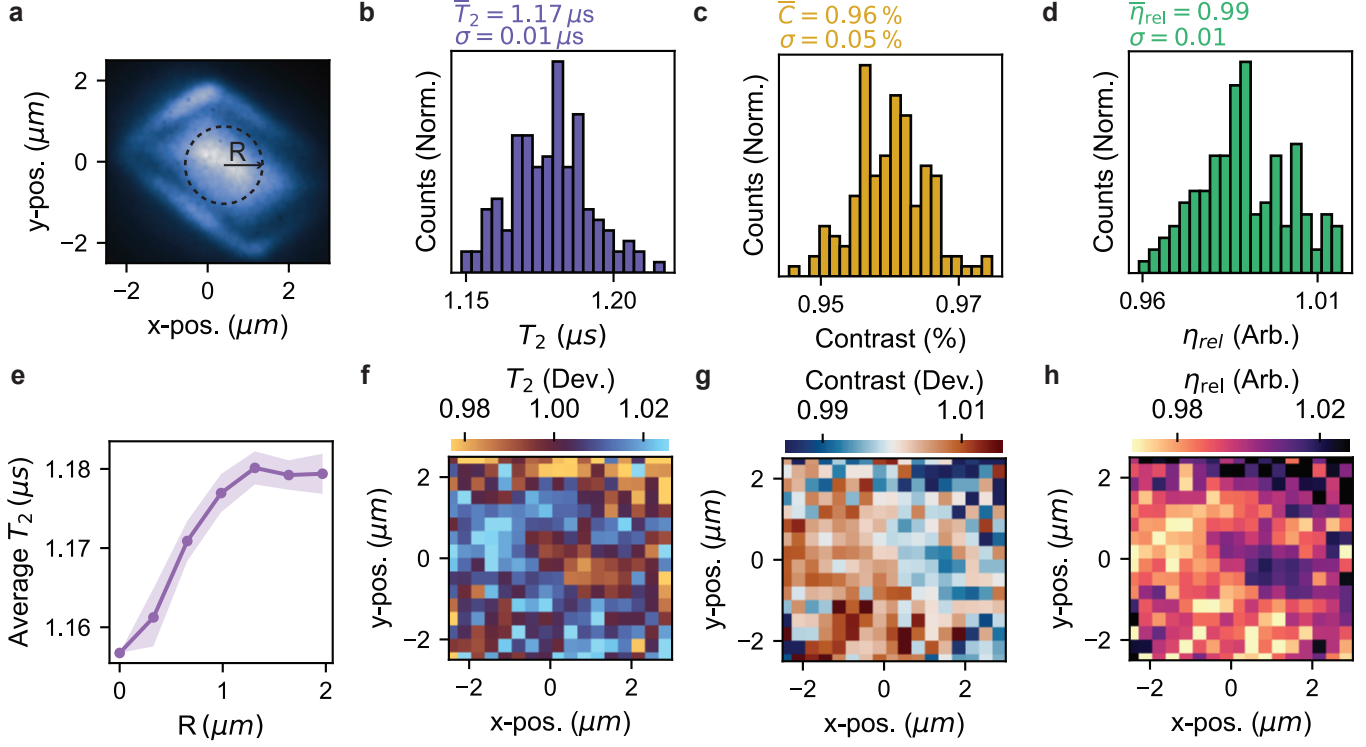


Figure 3: **Spatially resolved coherent control of a micro-crystal.** a) A photoluminescence image of the micro-crystal measured. b) Histogram of the coherence times measured within the same micro-crystal. c) Histogram of the measurement contrasts measured within the same micro-crystal. d) Histogram of the sensitivity scale factors measured within the same micro-crystal. e) Average coherence time as a function of radial distance (R) from the centre of the micro-crystal with errors represented by the shaded area. The radial distance is illustrated in figure a). f) Coherence time, T_2 , mapped for the micro-crystal. The data has been plotted as deviation from the mean to highlight variation. g) Spatially resolved measurement contrast (C) mapped as deviations for the micro-crystal. h) Sensitivity scale factor, η_{rel} , mapped as deviations across the micro-crystal.

can form well ordered crystalline environments could play a central role in unlocking a wider variety of spin-bearing molecules for quantum information science.

Finally, we use the contrast and the coherence time to spatially resolve the sensitivity in the crystalline micro-flake. The histogram of sensitivities in figure 3d shows an average sensitivity scale factor of 0.99 with variations in sensitivity of 1.3%. As expected from the reduced variation in both contrast and coherence time, we find that the sensitivity is much more uniform across the crystalline flake. Mapping the sensitivity in figure 3h, we see the same structure appearing as in the coherence map with the edge being more sensitive than the centre.

5 High-contrast optically detected coherent control of a nano-crystal

Motivated by the long coherence time and uniformity of the micro-crystal in figure 3, we next compare the optically detected coherent control of our bulk crystal to a single pentacene doped *p*-terphenyl nanocrystal. This is done by locating an isolated nanocrystal and switching our detection scheme to replace the camera with a single photon counting avalanche photo-detector. We also remove the lens which previously acted to focus the excitation on the back focal plane of our objective, allowing us to collect light from a single focused point. An image of the nanocrystal is shown in the inset of figure 4c.

First we measure Rabi oscillations using the pulse sequence in figure 4a. The oscillations for the bulk crystal are shown in figure 4b and the corresponding measurement for the nanocrystal can be seen in figure 4c. We are able to achieve measurement contrasts of 30% and 25% in the bulk and nanocrystal respectively. These measurements exceed previous reports using pc:ptp nanocrystals by 20%[18] and show only a 5% loss of contrast by reducing the crystal size below 1 μm .

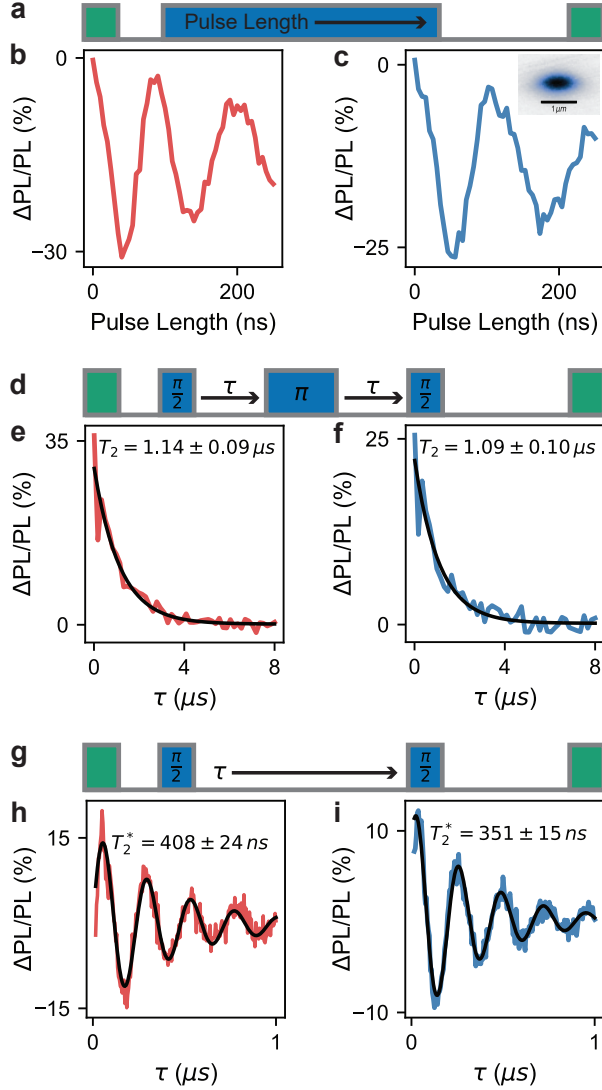


Figure 4: Optically detected magnetic resonance of a bulk and nano-crystal. a) Pulse sequence used for optically detected Rabi oscillations. b) Rabi oscillations measured on the bulk crystal with contrasts up to 30 %. c) Rabi oscillations measured on the nanocrystal with contrasts up to 25 %. d) Pulse sequence used for optically detected Hahn echo. e) Hahn echo measured on the bulk crystal with $1.14 \pm 0.09 \mu\text{s}$ coherence time and up to 35 % contrast. f) Hahn echo measured on the nano-crystal with $1.09 \pm 0.10 \mu\text{s}$ coherence time and up to 25 % contrast. g) Pulse sequence used for optically detected Ramsey fringes. h) Ramsey fringes measured on the bulk crystal with $T_2^* = 408 \pm 24 \text{ ns}$ and up to 30 % contrast. i) Ramsey fringes measured on the nano-crystal with $T_2^* = 351 \pm 15 \text{ ns}$ and up to 20 % contrast. All measurements were performed on the $|T_x\rangle \leftrightarrow |T_z\rangle$ transition under ambient conditions.

By changing the pulse sequence to a Hahn-echo we are able to study the coherence of the systems. Using the sequence in figure 4d, we measure the decays shown in figures 4e and f for the bulk and nano-crystal respectively. Here we have the same measurement contrasts as in the Rabi oscillations and a T_2 of $1.14 \pm 0.09 \mu\text{s}$ for the bulk crystal and $1.09 \pm 0.1 \mu\text{s}$ for the nanocrystal.

Using a Ramsey sequence (with a detuning of 5 MHz from the XZ transition) as in figure 4g we are able to measure the spin dephasing, T_2^* of the bulk and nano-crystals. The oscillation for the bulk crystal is shown in figure 4h with a contrast again of 30 % and $T_2^* = 408 \pm 24 \text{ ns}$. Figure 4i displays the Ramsey oscillations for the nanocrystal, here we have 20 % contrast and $T_2^* = 351 \pm 15 \text{ ns}$. Overall we find that even at quite high doping concentrations (0.1 % mol/mol) there is minimal impact on the contrast and coherence times of the molecular spins when reducing the

nanocrystal size to sub-micrometre scales. This is promising from both a sensing stand-point and for implementing recently proposed levitated optomechanics experiments with molecular nano-crystals[36].

With the contrast and coherence times measured we can then estimate the loss in sensitivity incurred by reducing the crystal size. For AC sensing the relevant measurement is the Hahn-echo, where the nano-crystal dropped by a factor of 0.83 in contrast and 0.96 in coherence time, hence the sensitivity of the nanocrystal is impaired by a factor of 1.2 (remembering sensitivity is like golf). Likewise for DC sensing the Ramsey measurement had a contrast decrease of 0.67 and a dephasing time decrease of 0.89, leading to a sensitivity scaling of 1.7.

6 Conclusion

Our work highlights the importance of understanding the effect of disorder within a quantum system on the coherence and contrast. Although the use of thin-films offers an approach to high-proximity sensing of both planar and non-planar structures, the introduced variability due to disorder will need to be accounted for when performing imaging using these materials. The increased uniformity of the micro-crystal, alongside the maintained coherence toward the edge of the flake offers an alternative to thin-films for high proximity sensing. Growing thin crystals[40, 46] on the surface of a sensing target could offer a higher performance alternative to thin-films. The micro- and nano-crystal results indicate that there is a much smaller impact on the coherence due to scaling down the crystal size than would be expected from solid state defects[27]. This suggests their future application as optically trapped sensors[38] for imaging and in spin-based optomechanical experiments[43]. We expect that finding novel methods to produce and place smaller doped molecular crystals to be a promising avenue for achieving higher resolution precision imaging.

7 Experimental methods

7.1 Film preparation

Thin films of p-terphenyl doped with pentacene were deposited onto quartz substrates via thermal co-evaporation of pentacene (Ossila, sublimated 99%) and *p*-terphenyl (TCI, >99%) under vacuum in a commercial thermal evaporator (Kurt J. Lesker). To ensure the correct doping ratio we calibrated the evaporation rates of both pentacene and *p*-terphenyl to ensure that the pentacene would evaporate at 0.1% of the *p*-terphenyl rate. The samples were then used unencapsulated and under ambient conditions.

7.2 Crystal growth and exfoliation

Crystals of p-terphenyl doped with pentacene were grown by solution recrystallization. Pentacene and p-terphenyl (0.1 mol %) were dissolved in dichlorobenzene at 160°C on a hotplate. The solution was then slowly cooled to room temperature over a period of 5 h, resulting in the formation of large crystals. The dichlorobenzene was subsequently decanted, and the crystals were washed with acetone to remove residual solvent before drying.

Micro-crystals were prepared by placing a single crystal in acetone and sonicating the suspension in an ultrasonic bath (VWR USC-THD Ultrasonic Cleaner) for 5 min. This process produced a stable suspension of micro-crystals in acetone. The micro-crystals were deposited onto quartz substrates by drop casting.

7.3 Continuous wave optically detected magnetic resonance

The sample is mounted between the poles of an electromagnet (Montana Instruments, Magneto-Optic Module) on a coplanar waveguide (CPW) which is used to generate microwave fields to drive resonance. The microwave signal is generated via a signal generator (Stanford Research Systems, SG396) and switched on and off at 211 Hz using a microwave switch (Minicircuits, ZYSWA-2-50DR+), driven by an arbitrary waveform generator (AWG) (Swabian, Pulse Streamer). We use 520 nm light from a solid-state laser (Hubner, Cobalt), which goes through a 550 nm short pass filter (Thorlabs, FESH550) before being focussed on the sample via a achromatic doublet (Thorlabs, AC254-035-B). The photoluminescence is collected via the same lens and split from the laser path using a dichroic beam splitter (Thorlabs, DMLP550R) and focused onto a silicon photoreceiver (Femto, OE200Si) via a matching achromatic doublet. The signal from the photoreceiver is monitored via a lock-in amplifier (Stanford Research Systems, SR865A), allowing measurement of the lockin signal and the constant photoluminescence during the magnetic field sweep.

7.4 Spatially resolved coherent control

The sample is mounted on a CPW which is used to generate microwave fields for coherent control. The excitation, from a 520 nm TTL controlled laser (Hubner, Cobolt 5051), is passed through a 550 nm short pass filter (Thorlabs, FESH550) and a biconvex lens (Thorlabs, LB1437) which is one focal length away from the back-focal plane of the objective. The excitation then goes to a dichroic beam splitter (Thorlabs, DMLP550R) before going to a 0.9 NA objective (Ziess, EC Epiplan-Neofluar 100x). The photoluminescence is collected through the same objective, passes through the dichroic and through an additional longpass filter (Thorlabs, FELH550). This filtered light is then passed through a 200 mm (Thorlabs, LB4282) lens and imaged onto a sCMOS camera (Andor, iStar sCMOS). The microwave signal is generated via a signal generator with built in quadrature modulation for phase control (Stanford Research Systems, SG396), with pulse gating achieved via a microwave switch (Minicircuits, ZYNSWA-2-50DR+) and amplification using a power amplifier (Minicircuits, HPA-272+). Timing control, used to pulse the laser and microwaves, as well as gate the camera is achieved using an AWG (Swabian, Pulse Streamer). Full details of the pulse sequences are outlined in our previous work[29].

7.5 Optically detected coherent control

For the nanocrystal and crystal measurement in figure 4 the excitation and collection paths are altered. We remove the biconvex lens, meaning that collimated light is input into the objective for a diffraction limited excitation spot. On the collection side the tube lens is removed and we use a fibre coupled single photon counting avalanche photodiode (SNAPD) (Excelitas, SPCM- AQRH-14-FC), with the filtered photoluminescence being focused onto a single mode fibre and input into the SNAPD. We use a event counter (Swabian, Time Tagger Ultra) to count the pulses from the SNAPD. Full pulse sequences used are available in the supplementary information.

7.6 Sensitivity Scale Factor and Data Analysis

As we are in the measurement regime where the measurement overhead is much longer than the coherence time, $t_{\text{overhead}} \gg T_2$, the sensitivity scales as $\eta_{\text{AC}}^v \propto \sqrt{t_{\text{overhead}}/CT_2\sqrt{n_{\text{av}}c_s}}$ [4]. Here C is the measurement contrast, T_2 is the coherence time, n_{av} is the doping ratio and c_s is the collection efficiency. Our experiments let us directly probe the variations in contrast and coherence time, so we can then use these with the above equation to calculate the variation in sensitivity. We do this by first scaling both the contrast and the coherence time, scaling them as $C^{\text{scale}}(i, j) = C(i, j)/C^{\text{av}}$ and $T_2^{\text{scale}}(i, j) = T_2(i, j)/T_2^{\text{av}}$ respectively. Then the sensitivity scaling factor, $\eta_{\text{rel}}^{(i, j)} = C^{\text{av}} \cdot T_2^{\text{av}} / C(i, j) \cdot T_2(i, j)$, which is effectively a measure of how the sensitivity is influenced by the variation in both the measurement contrast and coherence time.

We note that, for all analyses (including the contrast and coherence histograms), data points were removed based on the following criteria. First, points with poor fitting quality were excluded by applying a threshold of $r^2 < 0.85$. Second, outliers were removed by excluding values outside the 1st - 99th percentile range. Finally, for the microcrystal histograms in Fig. 3, data points lying outside the crystal were excluded using an intensity-based mask; a plot of this mask is provided in the Supplementary Materials.

7.6.1 Fitting Functions

Fitting is performed using the following functions:

$$\text{Hahn-Echo: } y = Ce^{-2\tau/T_2} + B$$

$$\text{Ramsey: } y = Ce^{-\tau/T_2^*} \cos(\omega\tau + \phi) + B$$

Author contributions

A.M, N.P.S and D.R.M contributed to the conceptualisation. A.M and N.P.S performed measurements and sample preparation. A.M and M.R.B analysed the data. A.M wrote the manuscript with inputs from all co-authors. Supervision, funding acquisition and resources were provided by D.R.M.

Acknowledgements

A.M is the recipient of an Office of National Intelligence National Intelligence Postdoctoral Grant (project number NIPG202510) funded by the Australian Government. N.P.S acknowledges the support from an Australian Government

Research Training Program (RTP) Scholarship. M.R.B acknowledges the support from the German Academic Exchange Service (DAAD) through the PROMOS scholarship.

Conflict of interest

The authors declare no potential conflict of interests.

References

- [1] G. Abrahams, A. Štuhec, V. Spreng, R. Henry, I. Kempf, J. James, K. Seckar, S. Stacey, V. Trelles-Fernandez, L. M. Antill, et al. Quantum spin resonance in engineered magneto-sensitive fluorescent proteins enables multi-modal sensing in living cells. *bioRxiv*, pages 2024–11, 2024.
- [2] C. G. Bailey, A. Mena, T. L. Leung, N. P. Sloane, C. Liao, D. R. McKenzie, D. R. McCamey, and A. W. Ho-Baillie. Revealing localized dark-exciton populations in 2d perovskites via magneto-optical microscopy. *Advanced Energy Materials*, page 2501593, 2025.
- [3] C. G. Bailey, N. P. Sloane, T. L. Leung, C. Liao, A. Mena, D. M. de Clercq, J. Yi, S. Palomba, M. P. Nielsen, D. R. McKenzie, et al. Between the nanosheets: Enhancing electron–hole exchange interaction for room-temperature magneto-photoluminescence in liquid-phase-exfoliated 2d perovskite. *ACS nano*, 2025.
- [4] J. F. Barry, J. M. Schloss, E. Bauch, M. J. Turner, C. A. Hart, L. M. Pham, and R. L. Walsworth. Sensitivity optimization for nv-diamond magnetometry. *Reviews of Modern Physics*, 92(1):015004, 2020.
- [5] M. S. Barson, L. M. Oberg, L. P. McGuinness, A. Denisenko, N. B. Manson, J. Wrachtrup, and M. W. Doherty. Nanoscale vector electric field imaging using a single electron spin. *Nano Letters*, 21(7):2962–2967, 2021.
- [6] S. Bayliss, D. Laorenza, P. Mintun, B. Kovos, D. Freedman, and D. Awschalom. Optically addressable molecular spins for quantum information processing. *Science*, 370(6522):1309–1312, 2020.
- [7] A. Bertran, K. B. Henbest, M. De Zotti, M. Gobbo, C. R. Timmel, M. Di Valentin, and A. M. Bowen. Light-induced triplet–triplet electron resonance spectroscopy. *The journal of physical chemistry letters*, 12(1):80–85, 2020.
- [8] R. Chowdhury, A. Inglis, L. E. Walker, P. Murto, C. Delpiano-Cordeiro, C. Morrison, N. A. Panjwani, Y. Fu, Y. Sun, W. Zhou, et al. Room temperature optical control of spin states in organic diradicals. *arXiv preprint arXiv:2510.09440*, 2025.
- [9] D. J. Christle, A. L. Falk, P. Andrich, P. V. Klimov, J. U. Hassan, N. T. Son, E. Janzén, T. Ohshima, and D. D. Awschalom. Isolated electron spins in silicon carbide with millisecond coherence times. *Nature materials*, 14(2):160–163, 2015.
- [10] M. W. Doherty, N. B. Manson, P. Delaney, F. Jelezko, J. Wrachtrup, and L. C. Hollenberg. The nitrogen-vacancy colour centre in diamond. *Physics Reports*, 528(1):1–45, 2013.
- [11] M. W. Doherty, V. V. Struzhkin, D. A. Simpson, L. P. McGuinness, Y. Meng, A. Stacey, T. J. Karle, R. J. Hemley, N. B. Manson, L. C. Hollenberg, et al. Electronic properties and metrology applications of the diamond nv- center under pressure. *Physical review letters*, 112(4):047601, 2014.
- [12] F. Dolde, H. Fedder, M. W. Doherty, T. Nöbauer, F. Rempp, G. Balasubramanian, T. Wolf, F. Reinhard, L. C. Hollenberg, F. Jelezko, et al. Electric-field sensing using single diamond spins. *Nature Physics*, 7(6):459–463, 2011.
- [13] J. S. Feder, B. S. Soloway, S. Verma, Z. Z. Geng, S. Wang, B. B. Kifle, E. G. Riendeau, Y. Tsaturyan, L. R. Weiss, M. Xie, et al. A fluorescent-protein spin qubit. *Nature*, 645(8079):73–79, 2025.
- [14] M. Fujiwara, S. Sun, A. Dohms, Y. Nishimura, K. Suto, Y. Takezawa, K. Oshimi, L. Zhao, N. Sadzak, Y. Umehara, et al. Real-time nanodiamond thermometry probing in vivo thermogenic responses. *Science advances*, 6(37):eaba9636, 2020.
- [15] X. Gao, S. Vaidya, S. Dikshit, P. Ju, K. Shen, Y. Jin, S. Zhang, and T. Li. Nanotube spin defects for omnidirectional magnetic field sensing. *Nature Communications*, 15(1):7697, 2024.
- [16] S. Gorgon, K. Lv, J. Grüne, B. H. Drummond, W. K. Myers, G. Londi, G. Ricci, D. Valverde, C. Tonnelé, P. Murto, et al. Reversible spin-optical interface in luminescent organic radicals. *Nature*, 620(7974):538–544, 2023.
- [17] A. Gottscholl, M. Kianinia, V. Soltamov, S. Orlinskii, G. Mamin, C. Bradac, C. Kasper, K. Krambrock, A. Sperlich, M. Toth, et al. Initialization and read-out of intrinsic spin defects in a van der waals crystal at room temperature. *Nature materials*, 19(5):540–545, 2020.

[18] H. Ishiwata, J. Song, Y. Shigeno, K. Nishimura, and N. Yanai. Molecular quantum nanosensors functioning in living cells. 2025.

[19] B. Kang, M. Jang, Y. Chung, H. Kim, S. K. Kwak, J. H. Oh, and K. Cho. Enhancing 2d growth of organic semiconductor thin films with macroporous structures via a small-molecule heterointerface. *Nature communications*, 5 (1):4752, 2014.

[20] S. M. Kopp, S. Nakamura, B. T. Phelan, Y. R. Poh, S. B. Tyndall, P. J. Brown, Y. Huang, J. Yuen-Zhou, M. D. Krzyaniak, and M. R. Wasielewski. Luminescent organic triplet diradicals as optically addressable molecular qubits. *Journal of the American Chemical Society*, 146(40):27935–27945, 2024.

[21] S. M. Kopp, S. Nakamura, Y. R. Poh, K. R. Peinkofer, B. T. Phelan, J. Yuen-Zhou, M. D. Krzyaniak, and M. R. Wasielewski. Optically detected coherent spin control of organic molecular color center qubits. *Journal of the American Chemical Society*, 2025.

[22] G. Kucsko, P. C. Maurer, N. Y. Yao, M. Kubo, H. J. Noh, P. K. Lo, H. Park, and M. D. Lukin. Nanometre-scale thermometry in a living cell. *Nature*, 500(7460):54–58, 2013.

[23] B. Li, G. Heller, J. Yong, A. Ungar, H. Tang, G. Wang, P. Hautle, Y. Quan, and P. Cappellaro. Robust ac vector sensing at zero magnetic field with pentacene. *arXiv preprint arXiv:2512.06272*, 2025.

[24] I. Lovchinsky, A. Sushkov, E. Urbach, N. P. de Leon, S. Choi, K. De Greve, R. Evans, R. Gertner, E. Bersin, C. Müller, et al. Nuclear magnetic resonance detection and spectroscopy of single proteins using quantum logic. *Science*, 351(6275):836–841, 2016.

[25] D. Lubert-Perquel, E. Salvadori, M. Dyson, P. N. Stavrinou, R. Montis, H. Nagashima, Y. Kobori, S. Heutz, and C. W. Kay. Identifying triplet pathways in dilute pentacene films. *Nature communications*, 9(1):4222, 2018.

[26] S. K. Mann, A. Cowley-Semple, E. Bryan, Z. Huang, S. Heutz, M. Attwood, and S. L. Bayliss. Chemically tuning room temperature pulsed optically detected magnetic resonance. *Journal of the American Chemical Society*, 2025.

[27] J. E. March, B. D. Wood, C. J. Stephen, L. D. Fervenza, B. G. Breeze, S. Mandal, A. M. Edmonds, D. J. Twitchen, M. L. Markham, O. A. Williams, et al. Long spin coherence and relaxation times in nanodiamonds milled from polycrystalline 12 c diamond. *Physical Review Applied*, 20(4):044045, 2023.

[28] A. Mena, R. Geng, W. Pappas, F. Maasoumi, and D. McCamey. Inter-and intra-device variation and correlation of hyperfine interactions in micron-scale organic light-emitting diodes. *Advanced Sensor Research*, 3(4):2300087, 2024.

[29] A. Mena, S. K. Mann, A. Cowley-Semple, E. Bryan, S. Heutz, D. R. McCamey, M. Attwood, and S. L. Bayliss. Room-temperature optically detected coherent control of molecular spins. *Physical review letters*, 133(12):120801, 2024.

[30] K. C. Miao, A. Bourassa, C. P. Anderson, S. J. Whiteley, A. L. Crook, S. L. Bayliss, G. Wolfowicz, G. Thiering, P. Udvarhelyi, V. Ivády, et al. Electrically driven optical interferometry with spins in silicon carbide. *Science Advances*, 5(11):eaay0527, 2019.

[31] W. J. Pappas, R. Geng, A. Mena, A. J. Baldacchino, A. Asadpoordarvish, and D. R. McCamey. Resolving the spatial variation and correlation of hyperfine spin properties in organic light-emitting diodes. *Advanced Materials*, 34(11):2104186, 2022.

[32] S. Scholten, G. Abrahams, B. Johnson, A. Healey, I. Robertson, D. Simpson, A. Stacey, S. Onoda, T. Ohshima, T. Kho, et al. Imaging current paths in silicon photovoltaic devices with a quantum diamond microscope. *Physical Review Applied*, 18(1):014041, 2022.

[33] H. Singh, N. D’Souza, K. Zhong, E. Druga, J. Oshiro, B. Blankenship, R. Montis, J. A. Reimer, J. D. Breeze, and A. Ajoy. Room-temperature quantum sensing with photoexcited triplet electrons in organic crystals. *Physical Review Research*, 7(1):013192, 2025.

[34] H. Singh, N. D’Souza, J. Garrett, A. Singh, B. Blankenship, E. Druga, R. Montis, L. Z. Tan, and A. Ajoy. High sensitivity pressure and temperature quantum sensing in pentacene-doped p-terphenyl single crystals. *Nature Communications*, 16(1):10530, 2025.

[35] D. J. Sloop, H.-L. Yu, T.-S. Lin, and S. Weissman. Electron spin echoes of a photoexcited triplet: Pentacene in p-terphenyl crystals. *The Journal of Chemical Physics*, 75(8):3746–3757, 1981.

[36] M. O. Steiner, J. S. Pedernales, and M. B. Plenio. Optically hyperpolarized materials for levitated optomechanics. *Quantum*, 9:1928, 2025.

[37] H. L. Stern, Q. Gu, J. Jarman, S. Eizagirre Barker, N. Mendelson, D. Chugh, S. Schott, H. H. Tan, H. Sirringhaus, I. Aharonovich, et al. Room-temperature optically detected magnetic resonance of single defects in hexagonal boron nitride. *Nature communications*, 13(1):618, 2022.

- [38] A. Stewart, Y. Zhu, Y. Liu, D. A. Simpson, and P. J. Reece. Optical tweezers assembled nanodiamond quantum sensors. *Nano Letters*, 24(39):12188–12195, 2024.
- [39] J.-P. Tetienne, N. Dortschuk, D. A. Broadway, A. Stacey, D. A. Simpson, and L. C. Hollenberg. Quantum imaging of current flow in graphene. *Science advances*, 3(4):e1602429, 2017.
- [40] S.-J. Wang, M. Sawatzki, H. Kleemann, I. Lashkov, D. Wolf, A. Lubk, F. Talnack, S. Mannsfeld, Y. Krupskaya, B. Büchner, et al. Vacuum processed large area doped thin-film crystals: A new approach for high-performance organic electronics. *Materials Today Physics*, 17:100352, 2021.
- [41] M. Wasielewski, S. Kopp, J. Palmer, B. Phelan, K. Peinkofer, S. Nakamura, M. Krzyaniak, et al. Molecular diradical spin qubits in a crystalline host as a platform for quantum sensing. 2026.
- [42] T. Wolf, P. Neumann, K. Nakamura, H. Sumiya, T. Ohshima, J. Isoya, and J. Wrachtrup. Subpicotesla diamond magnetometry. *Physical Review X*, 5(4):041001, 2015.
- [43] A. A. Wood, R. M. Goldblatt, R. E. Scholten, and A. M. Martin. Quantum control of nuclear-spin qubits in a rapidly rotating diamond. *Physical Review Research*, 3(4):043174, 2021.
- [44] A. A. Wood, D. J. McCloskey, N. Dortschuk, A. Lozovoi, R. M. Goldblatt, T. Delord, D. A. Broadway, J.-P. Tetienne, B. C. Johnson, K. T. Mitchell, et al. 3d-mapping and manipulation of photocurrent in an optoelectronic diamond device. *Advanced Materials*, 36(40):2405338, 2024.
- [45] K. Wu, S. Fan, Y. Zhang, W. Woudstra, T. Mulder, L. Boscher Navarro, J. van Dijken, K. Loos, and R. Schirhagl. Fluorescent nanodiamonds based theranostic platform for ph-sensitive drug delivery and quantum sensing. *Advanced Functional Materials*, page e14294, 2025.
- [46] Y. Wu and T. Weil. Recent developments of nanodiamond quantum sensors for biological applications. *Advanced Science*, 9(19):2200059, 2022.
- [47] Y. Zhang, A. Sigaeva, S. Fan, N. Norouzi, X. Zheng, I. Heijink, D. Slebos, S. Pouwels, and R. Schirhagl. Dynamics for high-sensitivity detection of free radicals in primary bronchial epithelial cells upon stimulation with cigarette smoke extract. *Nano Letters*, 24(31):9650–9657, 2024.